The Astrophysical Journal Letters, 916:L4 (9pp), 2021 July 20 https://doi.org/10.3847/2041-8213/ac0f02

# Electron Heat Flux Instabilities in the Inner Heliosphere: Radial Distribution and Implication on the Evolution of the Electron Velocity Distribution Function

Heyu Sun[1,2], Jinsong Zhao[1,2,3], Wen Liu[1,2], Yuriy Voitenko[4], Viviane Pierrard[4], Chen Shi[1,2], Yuhang Yao[1,2], Huasheng Xie[5,6], and Dejin Wu[1]
[1] Key Laboratory of Planetary Sciences, Purple Mountain Observatory, Chinese Academy of Sciences, Nanjing 210023, People's Republic of China; js_zhao@pmo.ac.cn
[2] School of Astronomy and Space Science,University of Science and Technology of China, Hefei 230026, People's Republic of China
[3] CAS Key Laboratory of Solar Activity, National Astronomical Observatories, Chinese Academy of Sciences, Beijing 100012, People's Republic of China
[4] Solar-Terrestrial Centre of Excellence, Space Physics Division, Royal Belgian Institute for Space Aeronomy, 3 av. Circulaire, B-1180, Brussels, Belgium
[5] Hebei Key Laboratory of Compact Fusion, Langfang 065001, People's Republic of China
[6] ENN Science and Technology Development Co., Ltd., Langfang 065001, People's Republic of China

*Received 2021 April 18; revised 2021 June 24; accepted 2021 June 25; published 2021 July 23*

## Abstract

This Letter investigates the electron heat flux instability using the radial models of the magnetic field and plasma parameters in the inner heliosphere. Our results show that both the electron acoustic wave and the oblique whistler wave are unstable in the regime with large relative drift speed ($\Delta V_e$) between electron beam and core populations. Landau-resonant interactions of electron acoustic waves increase the electron parallel temperature that would lead to suppressing the electron acoustic instability and amplifying the growth of oblique whistler waves. Therefore, we propose that the electron heat flux can effectively drive oblique whistler waves in an anisotropic electron velocity distribution function. This study also finds that lower-hybrid waves and oblique Alfvén waves can be triggered in the solar atmosphere, and that the former instability is much stronger than the latter. Moreover, we clarify that the excitation of lower-hybrid waves mainly results from the transit-time interaction of beaming electrons with resonant velocities $v_\parallel \sim \omega/k_\parallel$, where $\omega$ and $k_\parallel$ are the wave frequency and parallel wavenumber, respectively. In addition, this study shows that the instability of quasi-parallel whistler waves can dominate the regime with medium $\Delta V_e$ at the heliocentric distance nearly larger than 10 times of the solar radius.

*Unified Astronomy Thesaurus concepts:* Plasma astrophysics (1261); Space plasmas (1544); Solar wind (1534)

## 1. Introduction

The solar wind electron velocity distribution functions (eVDFs) normally consist of three populations: a relatively cool core, a hotter halo, and a highly energetic strahl (e.g., Feldman et al. 1975; Pilipp et al. 1987; Pierrard et al. 2001; Maksimovic et al. 2005; Marsch 2006; Štverák et al. 2009; Pulupa et al. 2014; Pierrard et al. 2016; Lazar et al. 2020). Both the strahl and halo are less dense than the core (e.g., Maksimovic et al. 2005; Štverák et al. 2009). Due to the strahl being more anisotropic than the halo, the electron heat flux is mainly carried by the strahl. Moreover, in situ solar wind observations have shown that the electron heat flux is limited below the values predicted from the Comlomb collision theory (Spitzer & Härm 1953). The electron heat flux can drive various kinetic instabilities (e.g., Gary et al. 1975, 1999; Volokitin & Krafft 2004; Tong et al. 2015; Shaaban et al. 2018; Verscharen et al. 2019; López et al. 2020; Sun et al. 2020), producing parallel and oblique whistler waves, oblique Alfvén waves, lower-hybrid waves, and electron acoustic (or beam) waves, and these instabilities can play significant roles in constraining the solar wind heat flux (e.g., Feldman et al. 1974; Gary & Feldman 1977; Verscharen et al. 2019; Halekas et al. 2020).

On the other hand, the electromagnetic waves driven by the electron heat flux instability can induce the scattering of field-aligned electrons toward an isotropic distribution (e.g., Vocks & Mann 2003; Pierrard et al. 2011; Boldyrev & Horaites 2019; Verscharen et al. 2019). The wave-particle interaction mechanism is usually thought to be one factor in forming the radial change of the halo and strahl densities (e.g., Maksimovic et al. 2005; Štverák et al. 2009; Lazar et al. 2020); that is, the relative density of the halo (strahl) increases (decreases) with the heliocentric distance, while total relative density of the halo and strahl nearly remains constant.

Recently, the role of the electron heat flux instability on the constraint of the solar wind heat flux and the scattering of highly energetic strahl have gained much attention (e.g., Kuzichev et al. 2019; López et al. 2019; Roberg-Clark et al. 2019; Shaaban et al. 2019; Vasko et al. 2019; Verscharen et al. 2019; López et al. 2020; Micera et al. 2020; Sun et al. 2020). Both theory and particle-in-cell (PIC) simulation results proposed that parallel whistler waves driven by the whistler heat flux instability seem unable to explain these two observational phenomena (e.g., Horaites et al. 2018; Kuzichev et al. 2019; Vasko et al. 2019; Verscharen et al. 2019; López et al. 2020). The oblique whistler waves self-generated by the heat flux instability are proposed to be a more plausible candidate (e.g., Kuzichev et al. 2019; Vasko et al. 2019; Verscharen et al. 2019; López et al. 2020). However, the oblique whistler heat flux instability can be much weaker than the electron acoustic (or beam) heat flux instability in the low-beta ($\beta_e \lesssim 1$) plasma environment (e.g., López et al. 2020; Sun et al. 2020), where $\beta_e$ is the ratio of the electron thermal to magnetic pressure. This conclusion comes from the instability analysis with varying $\beta_e$ where the magnetic field strength is fixed (Sun et al. 2020). To our knowledge, there is no work exploring the electron heat flux instabilities under the radial distributions of the magnetic field and plasma parameters in the inner heliosphere. As a consequence, a comprehensive distribution of the electron heat flux instability at different heliocentric distances is still unknown.

This study will explore the electron heat flux instability using the radial distributions of the magnetic field and plasma parameters in the inner heliosphere. The electron heat flux mainly drives four kinds of wave modes: electron acoustic (or beam) waves, lower-hybrid waves, oblique Alfvén waves, and whistler waves. The corresponding instabilities are classified into the electron acoustic heat flux instability (EA-HFI), the lower-hybrid heat flux instability (LH-HFI), the oblique Alfvén heat flux instability (OA-HFI), and the whistler heat flux instability (W-HFI). In order to distinguish W-HFI relating to (quasi-) parallel whistler waves from oblique whistler waves, we label the former as the parallel whistler heat flux instability (PW-HFI) and the latter as the oblique whistler heat flux instability (OW-HFI) in this study.

This Letter is organized as follows. Section 2 introduces the parameter models and presents the radial distribution of the electron heat flux instability in the inner heliosphere. Section 3 gives the estimation of the effective excitation and explores the evolution of eVDFs due to different kinds of wave-particle interactions. The discussion and summary are given in Section 4.

## 2. Radial Distribution of the Electron Heat Flux Instability

Similar to the electron model used in many previous works (e.g., Shaaban et al. 2019; López et al. 2020; Sun et al. 2020), we consider a two-component electron population consisting of core and beam components. These two electron components follow the drift Maxwellian distribution $f_s(v_\parallel, v_\perp) = \frac{N_s}{(\pi)^{3/2} V_{\mathrm{Ts}\parallel} V_{\mathrm{Ts}\perp}^2} \exp\left[-\frac{(v_\parallel - V_s)^2}{V_{\mathrm{Ts}\parallel}^2} - \frac{v_\perp^2}{V_{\mathrm{Ts}\perp}^2}\right]$, where $v_\parallel$ and $v_\perp$ are electron velocities parallel and perpendicular to the magnetic field, respectively. $N_s$, $V_s$, $V_{\mathrm{Ts}\parallel} = \sqrt{2T_{s\parallel}/m_s}$, $V_{\mathrm{Ts}\perp} = \sqrt{2T_{s\perp}/m_s}$, $m_s$, $T_{s\parallel}$, and $T_{s\perp}$ denote the number density, the drift speed, the parallel thermal speed, the perpendicular thermal speed, the mass, the parallel and perpendicular temperature for the species "s" ("ec" for the core and "eb" for the beam), respectively. This study will mainly consider the isotropic temperature case, that is, $T_{s\parallel} = T_{s\perp} = T_s$. Consequently, the electron heat flux is contributed by both core and beam components, i.e., $q_e = N_{\mathrm{ec}} V_{\mathrm{ec}} (5T_{\mathrm{eb}} + m_e V_{\mathrm{eb}}^2 - 5T_{\mathrm{ec}} - m_e V_{\mathrm{ec}}^2)/2$ (e.g., Gary et al. 1999). This study also considers a zero electron current condition, i.e., $N_{\mathrm{ec}} V_{\mathrm{ec}} + N_{\mathrm{eb}} V_{\mathrm{eb}} = 0$, in the proton frame where protons follow the Maxwellian distribution with no drift speed $V_p = 0$.

The heat flux instability can be driven by a strong electron heat flux (e.g., Feldman et al. 1975). In order to exhibit the radial distributions of such instability, we use the magnetic field strength and plasma parameter models summarized in Bale et al. (2016). The radial distribution of the total electron number density $N_e = N_{\mathrm{ec}} + N_{\mathrm{eb}}$ is

$$N_e(r) = N_0 \times \exp\left(\frac{3.67 R_S}{r}\right) \times \left(\frac{R_S^2}{r^2} + \frac{4.9 R_S^3}{r^3} + \frac{7.6 R_S^4}{r^4} + \frac{6.0 R_S^5}{r^5}\right), \tag{1}$$

where $N_0 = 3.26 \times 10^5\ \mathrm{cm}^{-3}$, $r$ is the heliocentric distance, and $R_S$ is the solar radius. The radial distribution of the proton temperature is

$$T_p(r) = \frac{226.4}{(r/R_S)^{0.6}}\ [\mathrm{eV}], \tag{2}$$

The radial distribution of the magnetic field strength is

$$B_0(r) = \frac{860 R_S}{r} \sqrt{\left(\frac{215 R_S}{r}\right)^2 + \left(\frac{405}{V_{\mathrm{sw}}}\right)^2}\ [\mathrm{nT}], \tag{3}$$

with the radial distribution of the solar wind velocity

$$V_{\mathrm{sw}}(r) = 430 \sqrt{1 - \exp\left(-\frac{r/R_S - 2.8}{25}\right)}\ [\mathrm{km/s}]. \tag{4}$$

According to the relative density ∼0.02–0.1 and relative temperature ∼3–10 between core and suprathermal electron components in the solar wind at $r \sim 0.3$–3 au (Štverák et al. 2009; Pierrard et al. 2016), we assume $N_{\mathrm{eb}} = N_e - N_{\mathrm{ec}} = 0.05 N_e$ and $T_{\mathrm{eb}} = 5T_{\mathrm{ec}} = 5T_p$ at arbitrary heliocentric distance. Actually, $N_{\mathrm{eb}}/N_e$ and $T_{\mathrm{eb}}/T_{\mathrm{ec}}$ are different at varying heliocentric distances. Moreover, a recent analysis for the electron data measured by the Parker Solar Probe has revealed the suprathermal density fraction ∼0.015 that is lower than the value used in present study (Halekas et al. 2020). Therefore, this Letter provides a preliminary understanding for the radial distribution of the heat flux instability in the inner heliosphere.

Using the aforementioned plasma and magnetic field parameters, we explore the electron heat flux instability in the inner heliosphere under the plasma kinetic model. The plasma wave eigenmodes and their instabilities correspond to solutions of the wave equation $c^2 \boldsymbol{k} \times (\boldsymbol{k} \times \boldsymbol{E}) + \omega^2 \boldsymbol{\epsilon} \cdot \boldsymbol{E} = 0$ derived from the linear Vlasov–Maxwell equations (e.g., Stix 1992), where $\boldsymbol{k}$ denotes the wavevector, $\omega$ denotes the wave frequency, $c$ is the light speed, $\boldsymbol{\epsilon}$ denotes the dielectric tensor, and $\mathbf{E}$ is the wave electric field. In order to obtain the strongest instability with varying heliocentric distance and $V_{\mathrm{eb}}$, we use a newly developed numerical solver BO/PDRK, which has been proven to be a useful tool in investigating plasma waves and instabilities (Xie 2019; Sun et al. 2019, 2020; Shi et al. 2020; Xie et al. 2021).

Figures 1(a)–(f) present the radial distributions of the growth rate $\gamma$, the real wave frequency $\omega_r$, the wavenumber $\lambda_e k$, the wave normal angle $\theta$, and the argument $\arg(E_y/E_x)$ and absolute value $|E_y/E_x|$ of the ratio between two perpendicular electric field fluctuations $E_x$ and $E_y$ at positions of the strongest electron heat flux instability. There are four kinds of electron heat flux instabilities: EA-HFI, LH-HFI, OA-HFI, and PW-HFI, and they are labeled as "I", "II", "III", and "IV" in Figure 1(a), respectively. These four instabilities dominate different $r - V_{\mathrm{eb}}$ regions. EA-HFI controls the electron heat flux instability at large $V_{\mathrm{eb}}$ ($\gtrsim 1.0$–$2.5 V_{\mathrm{Ae}}$), which is consistent with results given by López et al. (2020) and Sun et al. (2020).

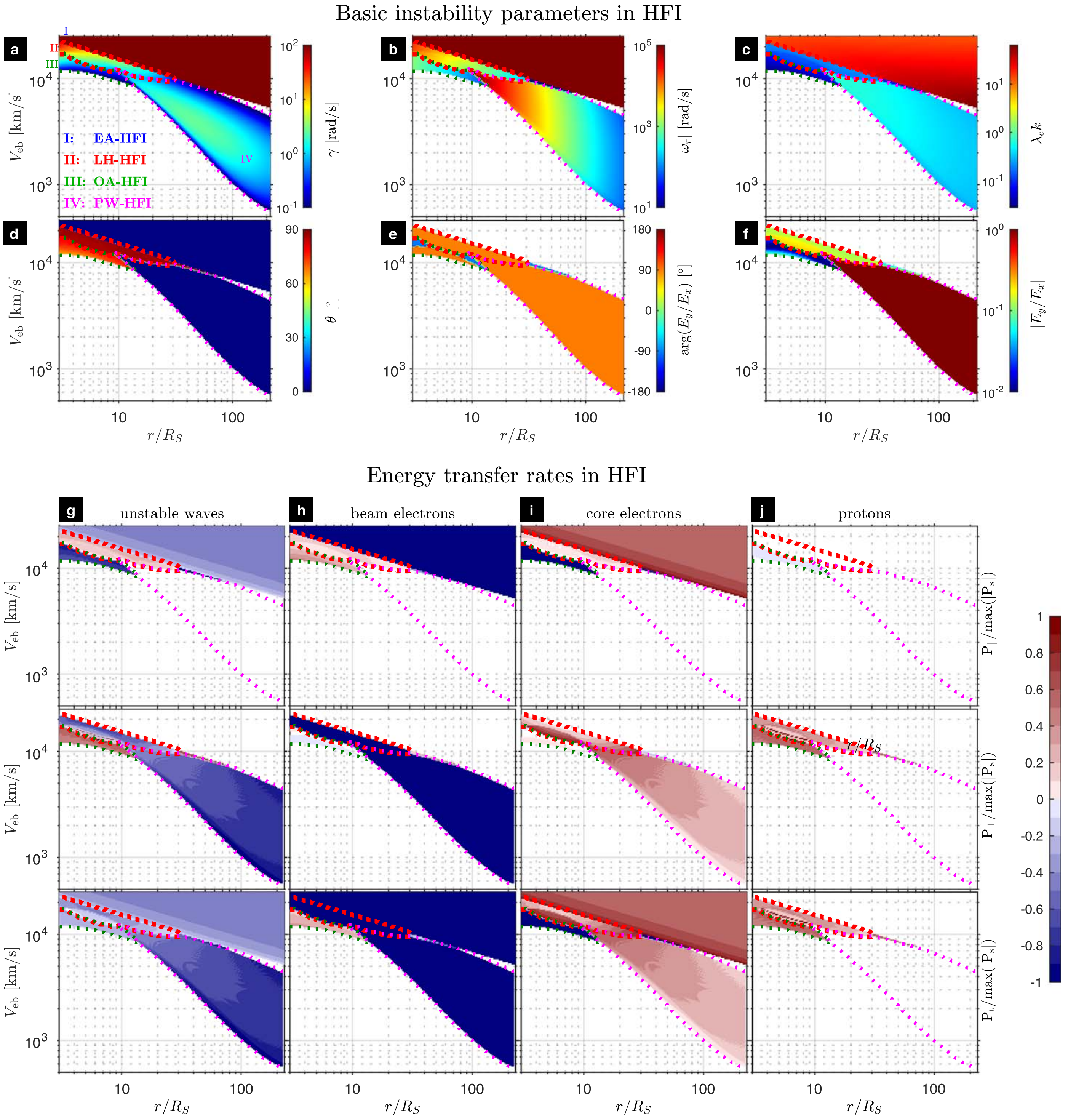

**Figure 1.** $r$–$V_{\rm eb}$ distributions of basic instability parameters and energy transfer rates in the inner heliosphere. (a) The growth rate $\gamma$, (b) the real wave frequency $\omega_r$, (c) the wavenumber $k$ normalized by the electron inertial length $\lambda_e$, (d) the wave normal angle $\theta$, (e) the argument of the ratio between two perpendicular electric field $\arg(E_y/E_x)$, (f) $|E_y/E_x|$, (g) the net energy transfer rate, (h) the energy transfer rate of beam electrons, (i) the energy transfer rate of core electrons, and (j) the energy transfer rate of protons at positions of the strongest electron heat flux instability. Upper, middle and bottom panels in Figures (g)–(j) denote the parallel, perpendicular, and total energy transfer rate, respectively. The red, green, and magenta dotted curves denote boundaries of LH-HFI, OA-HFI, and PW-HFI, respectively. The unstable regime beyond LH-HFI, OA-HFI, and PW-HFI is the regime controlled by EA-HFI. The data with $\gamma < 0.1$ rad s$^{-1}$ are removed.

Here $V_{\rm Ae} = B_0 \big/ \sqrt{\mu_0 m_e N_e}$ is calculated at the corresponding heliocentric distance $r$, and consequently $V_{\rm Ae}$ decreases with $r$, where $\mu_0$ is the permeability of free space. LH-HFI and OA-HFI dominate the regime with $r \lesssim 30 R_S$ and $V_{\rm eb} \sim 0.5$–$1.1 V_{\rm Ae}$ and the regime with $r \lesssim 13 R_S$ and $V_{\rm eb} \sim 0.4$–$0.6 V_{\rm Ae}$, respectively. PW-HFI can arise in the regime where $r \gtrsim 10 R_S$ and $V_{\rm eb} \sim 0.3$–$2.3 V_{\rm Ae}$. Moreover, the growth rates in EA-HFI and PW-HFI are maximum at $\theta = 0°$, and the strongest LH-HFI and OA-HFI arise in oblique propagating directions, i.e., the former at $\theta \sim 87°$ and the latter at $\theta \sim 74°$. More differences among these four instabilities are evident in Table 1, which summarizes the characteristic parameters shown in Figure 1.

**Table 1**
Characteristic Parameters in the Strongest Electron Heat-flux Instability in the Inner Heliosphere[a]

| | EA-HFI | LH-HFI | OA-HFI | PW-HFI |
|---|---|---|---|---|
| $r$ | no limitation | $\lesssim 30R_S$ | $\lesssim 13R_S$ | $\gtrsim 10R_S$ |
| $V_{\rm eb}$ | $\gtrsim 1.0$–$2.5V_{\rm Ae}$ | 0.5–$1.1V_{\rm Ae}$ | 0.4–$0.6V_{\rm Ae}$ | 0.3–$2.3V_{\rm Ae}$ |
| $\gamma$ | $\sim 0.1\Omega_{\rm pe}$ | $\sim 0.01\Omega_{\rm cp}$ | $\sim 7\times 10^{-4}\Omega_{\rm cp}$ | $\sim 5\Omega_{\rm cp}$ |
| $\omega_r$ | $\sim 1.6\Omega_{\rm pe}$ | $\sim 8\Omega_{\rm cp}$ | $\sim -0.5\Omega_{\rm cp}$[b] | $\sim 300\Omega_{\rm cp}$ |
| $\arg(E_y/E_x)$ | only $E_z$ | 90° | ~21° | 90° |
| $\lvert E_y/E_x\rvert$ | only $E_z$ | ~0.16 | ~0.02 | 1 |
| $\lambda_e k$ | ~22 | ~0.17 | ~0.05 | ~0.43 |
| $\theta$ | 0° | ~87° | ~73° | 0° |
| $\overline{P}_{\rm eb}$ | −1 | −1 | 0.25 ± 0.05 | −1 |
| $\overline{P}_{\rm eb\perp}$ | 0 | −1.10 ± 0.02 | −0.04 ± 0.03 | −1 |
| $\overline{P}_{\rm eb\parallel}$ | −1 | 0.10 ± 0.02 | 0.28 ± 0.08 | 0 |
| $\overline{P}_{\rm ec}$ | 0.60 ± 0.10 | 0.47 ± 0.23 | −1 | 0.29 ± 0.12 |
| $\overline{P}_{\rm ec\perp}$ | 0 | 0.41 ± 0.25 | 0.02 ± 0.02 | 0.29 ± 0.12 |
| $\overline{P}_{\rm ec\parallel}$ | 0.60 ± 0.10 | 0.07 ± 0.05 | −1.01 ± 0.02 | 0 |
| $\overline{P}_p$ | 0 | 0.34 ± 0.26 | 0.51 ± 0.02 | 0 |
| $\overline{P}_{\rm p\perp}$ | 0 | 0.34 ± 0.26 | 0.52 ± 0.02 | 0 |
| $\overline{P}_{\rm p\parallel}$ | 0 | 0 | −0.01 ± 0.001 | 0 |
| $\overline{P}_t$ | −0.40 ± 0.10 | −0.25 ± 0.12 | −0.25 ± 0.03 | −0.71 ± 0.12 |
| $\overline{P}_{\rm t\perp}$ | 0 | −0.35 ± 0.37 | 0.50 ± 0.04 | −0.71 ± 0.12 |
| $\overline{P}_{\rm t\parallel}$ | −0.40 ± 0.10 | 0.16 ± 0.06 | −0.75 ± 0.06 | 0 |

**Notes.**

[a] $\overline{P} = P/\max(|P_s|)$, in which $\max(|P_s|)$ corresponds to the magnitude of the energy transfer rate of the particle species being the main source of the instability, i.e., the electron beam in EA-HFI, LH-HFI, and PW-HFI and the electron core in OA-HFI. $\overline{P}$ is normally given by using the mean and standard deviation.

[b] The negative sign of $\omega_r$ denotes the wave propagating against the background magnetic field.

On the other hand, in order to explore the energy transfer between unstable waves and each particle species (e.g., Stix 1992; Quataert 1998; He et al. 2019; Klein et al. 2019), we calculate the energy transfer rate defined as

$$P_s = \frac{\boldsymbol{E}\cdot\boldsymbol{J}_s^{*} + \boldsymbol{E}^{*}\cdot\boldsymbol{J}_s}{\epsilon_0|\boldsymbol{E}|^2 + |\boldsymbol{B}|^2/\mu_0}, \tag{5}$$

where the plasma current $\boldsymbol{J}_s$ is given by $\boldsymbol{J}_s = \boldsymbol{\sigma}_s\cdot\boldsymbol{E}$, $\boldsymbol{\sigma}_s$ is the conductivity tensor, $\epsilon_0$ is permittivity of free space, and the superscript "*" denotes the complex conjugate. $P_s$ can be decomposed as contributions from parallel and perpendicular electric field,

$$P_{\rm s\parallel} = \frac{\boldsymbol{E}_\parallel\cdot\boldsymbol{J}_{\rm s\parallel}^{*} + \boldsymbol{E}_\parallel^{*}\cdot\boldsymbol{J}_{\rm s\parallel}}{\epsilon_0|\boldsymbol{E}|^2 + |\boldsymbol{B}|^2/\mu_0}, \tag{6}$$

and

$$P_{\rm s\perp} = \frac{\boldsymbol{E}_\perp\cdot\boldsymbol{J}_{\rm s\perp}^{*} + \boldsymbol{E}_\perp^{*}\cdot\boldsymbol{J}_{\rm s\perp}}{\epsilon_0|\boldsymbol{E}|^2 + |\boldsymbol{B}|^2/\mu_0}. \tag{7}$$

A sum of the energy transfer rate of each particle species (i.e., $\sum P_{s,{\rm s}\parallel,{\rm s}\perp}$) represents the net energy transfer rate between unstable waves and particles. Moreover, the relation of $\sum P_s = -2\gamma$ is always satisfied.

The radial distributions of the net energy transfer rate of unstable waves and energy transfer rates of each particle species are shown in Figures 1(g)–(j). In the strongest EA-HFI (PW-HFI), the parallel (perpendicular) electric field is responsible for the energy transfer, where the electron beam releases the free energy to unstable waves, and the electron core gains energy from unstable waves. In the strongest LH-HFI, the electron beam releases the free energy through perpendicular electric field, and the electron core and proton populations also gain energy through perpendicular electric field. In the strongest OA-HFI, the electron core releases the free energy in parallel direction due to parallel electric field, and most of energy of unstable waves flows into the proton and electron beam populations in sequence. Therefore, Figures 1(g)–(j) clearly exhibit that different electron heat flux instabilities result in different energy transfers between unstable waves and particles in the inner heliosphere (see also Table 1).

## 3. Effective Excitation and Implication on the Evolution of the Electron Velocity Distribution Function

In reality, because the electron beam can suffer highly structured plasma environment as it propagates outward from the Sun, the plasma environment cannot always support the excitation of the heat flux instability; this results in the problem of the effective excitation of unstable waves. In order to proceed with an estimation of the effective excitation, we assume that the wave amplitude is continuously growing, i.e., $E_t = E_0\exp(\gamma t)$, which indicates the instability staying in a linear stage. The linear growth time is estimated as $t_{\rm grow} = \ln(E_t/E_0)/\gamma$, where $E_0$ is the wave amplitude at an initial time of the instability, and $E_t$ is the wave amplitude after $t_{\rm grow}$. On the other hand, the propagating time of the electron beam through the structured plasma environment can be qualitatively estimated by $t_{\rm prop} = L/V_{\rm eb}$, where $L$ represents the characteristic spatial scale of the structured plasma environment. Here we use $L(r) = \sqrt{B_0(r_0)/B_0(r)}\,L(r_0)$ resulting from the radial expansion effect, where $B_0(r_0)$ and $L(r_0)$ are magnetic field and characteristic spatial scale at $r_0 = 2.8R_S$ (according to Equation (4)).

Comparing $t_{\rm grow}$ with $t_{\rm prop}$, we can simply estimate whether or not the instability excitation is effective. $t_{\rm grow}/t_{\rm prop} < 1$

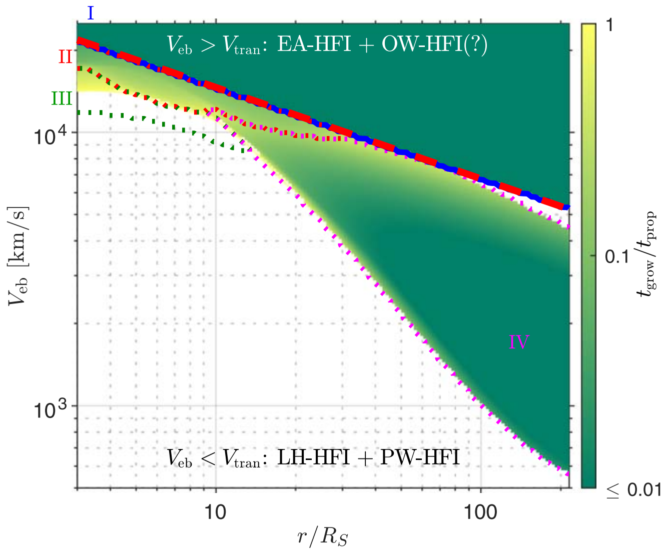

**Figure 2.** Radial distribution of the ratio ($t_{\rm grow}/{\rm t_{prop}}$) of the linear growth time $t_{\rm grow}$ to electron beam propagation time $t_{\rm prop}$. The data with $t_{\rm grow}/t_{\rm prop} > 1$ and $\gamma < 0.1$ rad/s are removed. The blue line denotes the boundary of EA-HFI, which is fitted by $V_{\rm tran} = 1.\ 3V_{\rm Teb}$ (red dashed line). The electron dynamics is mainly controlled by EA-HFI and OW-HFI in the $V_{\rm eb} > {\rm V_{tran}}$ regime and by LH-HFI and PW-HFI in the $V_{\rm eb} < {\rm V_{tran}}$ regime.

corresponds to the effective excitation. Figure 2 presents the radial distribution of $t_{\rm grow}/t_{\rm prop}$ at $E_t/E_0 = 10^4$ and $L(r_0) = R_S$. This figure shows that EA-HFI, LH-HFI, and PW-HFI can be efficiently excited, and OA-HFI is efficiently growing in the region very close to the Sun. If we assume $L(r) = R_S$ (not shown), the effective growing regions of LH-HFI and PW-HFI shrink due to shorter $t_{\rm prop}$.

On the basis of Figure 2, we classify the electron beam drift velocity into two regimes, i.e., the $V_{\rm eb} > V_{\rm tran}$ regime and the $V_{\rm eb} < V_{\rm tran}$ regime, where $V_{\rm tran} \sim 1.3V_{\rm Teb}$ corresponds to the velocity threshold of EA-HFI. Because the eVDF can considerably evolve through wave-particle interaction mechanisms, we will discuss its evolution during the heat flux instability in the $V_{\rm eb} > V_{\rm tran}$ and $V_{\rm eb} < V_{\rm tran}$ regime, respectively.

### 3.1. Evolution of eVDFs in the $\mathrm{V}_{eb} > \mathrm{V}_{tran}$ Regime

In the $V_{\rm eb} > V_{\rm tran}$ regime, in addition to EA-HFI, other kinds of instabilities (e.g., OW-HFI, LH-HFI, OA-HFI, and firehose heat flux instability) can arise (e.g., Shaaban et al. 2019; López et al. 2020; Sun et al. 2020). OW-HFI is recently proposed as the best candidate to scatter the strahl into halo, therefore it is interesting to explore the competition between EA-HFI and OW-HFI under different plasma conditions. Here we focus on the effect of the electron temperature that is significantly affected by EA-HFI.

In order to demonstrate the coexistence of both EA-HFI and OW-HFI, we checked the dependence between the heat flux instability and the beaming electron speed by using the magnetic field and plasma parameters at $r = 55R_S$ and found that OW-HFI can arise as $V_{\rm eb} \gtrsim 1.4 \times 10^4$ km s$^{-1}$. An example of the coexistence of EA-HFI and OW-HFI is given in Figure 3(a), which presents the $k$–$\theta$ distributions of these two instabilities at $V_{\rm eb} = 1.5 \times 10^4$ km s$^{-1}$ and $r = 55R_S$. EA-HFI is much stronger than OW-HFI as the initial electron temperatures are isotropic, and therefore the former instability controls the electron dynamics. We note that in addition to EA-HFI and OW-HFI, there are other kinds of weaker heat flux instabilities (e.g., LH-HFI and firehose heat flux instability) with $\gamma/\Omega_{\rm cp} < 1$.

Figures 3(b) and (c) present the dependence of the electron heat flux instability on parallel temperature anisotropies ($A_{\rm eb} \equiv T_{\rm eb\|}/T_{\rm eb\perp} - 1$ and $A_{\rm ec} \equiv T_{\rm ec\|}/T_{\rm ec\perp} - 1$). Figure 3(b) shows that with increasing $A_{\rm eb}$ and/or $A_{\rm ec}$, the growth rate of EA-HFI decreases, and this instability is totally suppressed at larger $A_{\rm eb}$ and/or $A_{\rm ec}$. Figure 3(c) considers a hotter electron core case $T_{\rm ec\perp} = 2T_p$, and this figure shows that EA-HFI disappears at medium parallel temperature anisotropy; this is because hotter core electrons result in more strong Landau damping, which can extinguish EA-HFI.

Different from EA-HFI, OW-HFI arises at large $A_{\rm eb}$ and $A_{\rm ec}$. Also, OW-HFI normally enhances with increasing $A_{\rm eb}$ and $A_{\rm ec}$. From the analysis of the energy transfer rate, we find that the enhancement of OW-HFI in plasmas with the parallel electron temperature anisotropy is mainly contributed by $n = -1$ cyclotron-resonant interaction with core electrons and $n = 1$ cyclotron-resonant interactions with beam electrons. The latter mechanism would result in the formation of an electron population with isotropic temperatures, which is proposed as one mechanism responsible for scattering the strahl into halo in the solar wind (Verscharen et al. 2019).

Based on Figures 3(a)–(c), Figure 3(d) gives a sketch of the evolution of eVDFs consisting of core and beam (drifting at $V_{\rm eb} > {\rm V_{tran}}$) components. EA-HFI was initially triggered as both core and beam have isotropic temperatures. The excited quasi-electrostatic electron acoustic waves can heat both core and beam electrons during and after EA-HFI, resulting in a parallel temperature anisotropy that could favor the excitation of OW-HFI. Then OW-HFI would scatter beam electrons along the diffusion path as proposed by Verscharen et al. (2019). The similar process was explored in a PIC simulation performed by An et al. (2017), who found that both EA-HFI and OW-HFI can arise during the development of a beam ring electron in a plasma with medium $\Omega_{\rm pe}/|\Omega_{\rm ce}|$, where $\Omega_{\rm pe}$ denotes the electron plasma frequency, and $\Omega_{\rm ce}$ is the electron cyclotron frequency. Furthermore, Micera et al. (2020) confirmed the broadening of the pitch angle distribution of the strahl during OW-HFI via PIC simulations of W-HFI.

It should be noted that we also explored the dependence of the heat flux instability on $A_{\rm eb}$ and $A_{\rm ec}$ at $r = 215R_S$ and $V_{\rm eb} = 6 \times 10^3$ km s$^{-1}$ (not shown), which yields conclusions consistent with that summarized in Figure 3.

### 3.2. Evolution of eVDFs in the $\mathrm{V}_{eb} < V_{tran}$ Regime

In the $V_{\rm eb} < V_{\rm tran}$ regime, LF-HFI or PW-HFI mainly determines the evolution of eVDFs.

LH-HFI can control the electron dynamics in the low-$\beta_e$ plasma. Before we proceed to analyze how wave-particle interaction mechanisms affect the eVDF during LH-HFI, we will give a comprehensive overview of LH-HFI, as shown in Figure 4(a). This figure presents the distributions of the growth rate $\gamma$ and the real frequency $\omega_r$ at $V_{\rm eb} = 1.5 \times 10^4$ km s$^{-1}$ and $r = 10R_S$. The $k - \theta$ distributions show that in addition to LH-HFI that resides in a narrow angle region, $\theta \sim 86°$–$88°$, OA-HFI distributes in a broad angle region, $\theta \sim 45°$–$89°$. The maximum growth rate in LH-HFI is nearly three times larger than OA-HFI. Furthermore, the distributions at $\theta = 87°$ further show that $\gamma$ is suppressing and $\omega_r$ is cut off at $n\Omega_{\rm cp}$ ($n = 1$, 2...12), and the reason for these features is due to the cyclotron

(a) HFI at $V_{\rm eb} = 1.5 \times 10^4$ km/s and $r = 55R_S$

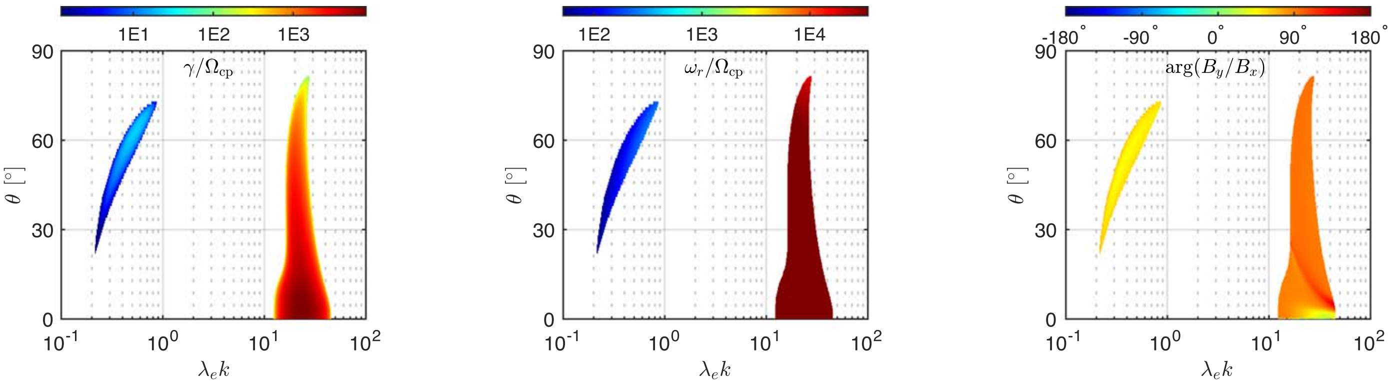

(b) HFI as functions of $A_{\rm eb}$ and $A_{\rm ec}$ at $T_{\rm eb\perp} = 5T_{\rm ec\perp} = 5T_p$

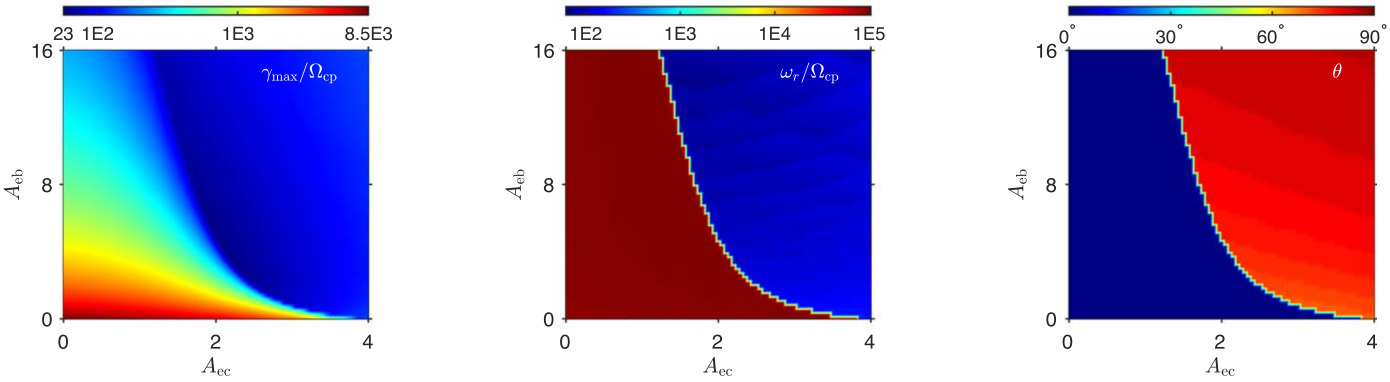

(c) HFI as functions of $A_{\rm eb}$ and $A_{\rm ec}$ at $T_{\rm eb\perp} = 2.5T_{\rm ec\perp} = 5T_p$

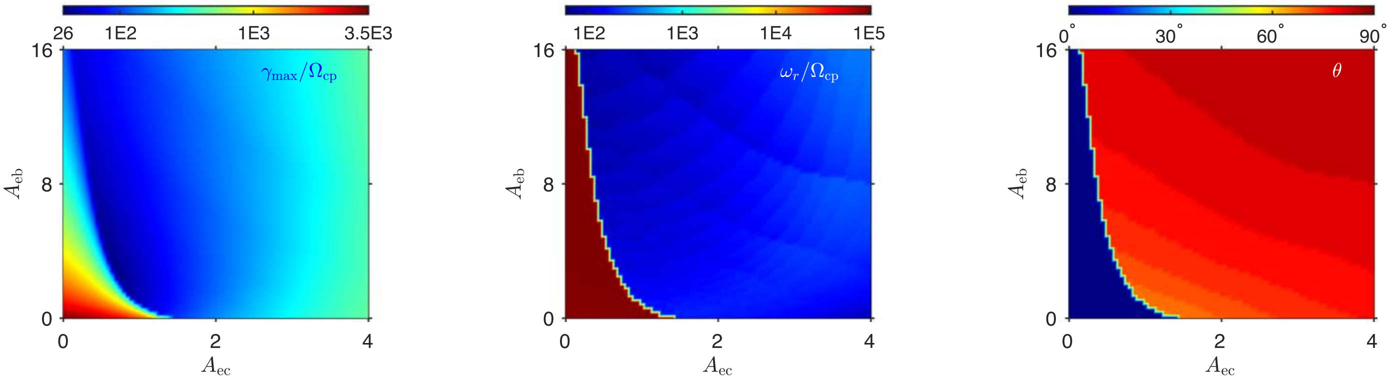

(d) Excitation of EA-HFI and OW-HFI under different eVDFs

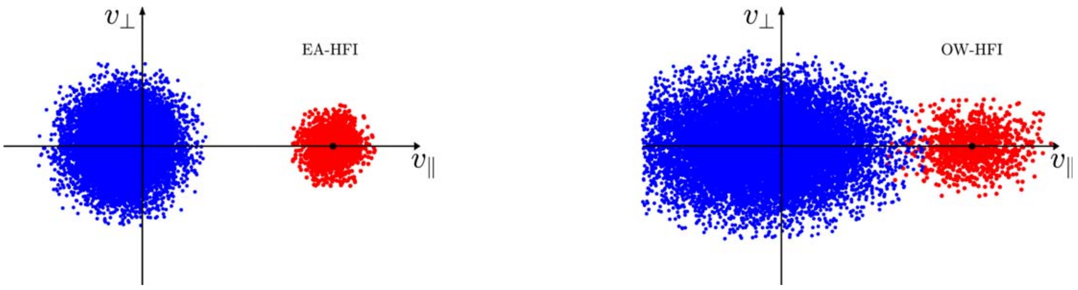

**Figure 3.** (a) Distributions of the growth rate $\gamma$, the real wave frequency $\omega_r$, and the argument of the ratio between two perpendicular magnetic field $\arg(B_y/B_x)$ in the electron heat flux instability at $V_{\rm eb} = 1.5 \times 10^4$ km s$^{-1}$ and $r = 55R_s$. (b) $\gamma$, $\omega_r$, and the wave normal angle $\theta$ as functions of $A_{\rm eb}$ and $A_{\rm ec}$ in the strongest heat flux instability occurring at $T_{\rm eb\perp} = T_{\rm ec\perp} = 5T_p$. (c) $\gamma$, $\omega_r$ and $\theta$ as functions of $A_{\rm eb}$ and $A_{\rm ec}$ in the strongest heat flux instability occurring at $T_{\rm eb\perp} = 2.5T_{\rm ec\perp} = 5T_p$. (d) The excitation of EA-HFI and OW-HFI under different eVDFs: EA-HFI preferentially triggered in eVDF with isotropic temperatures, and OW-HFI preferentially triggered in eVDF with anisotropic temperatures.

(a) LH-HFI at $V_{\rm eb} = 1.5 \times 10^4$ km/s and $r = 10R_S$

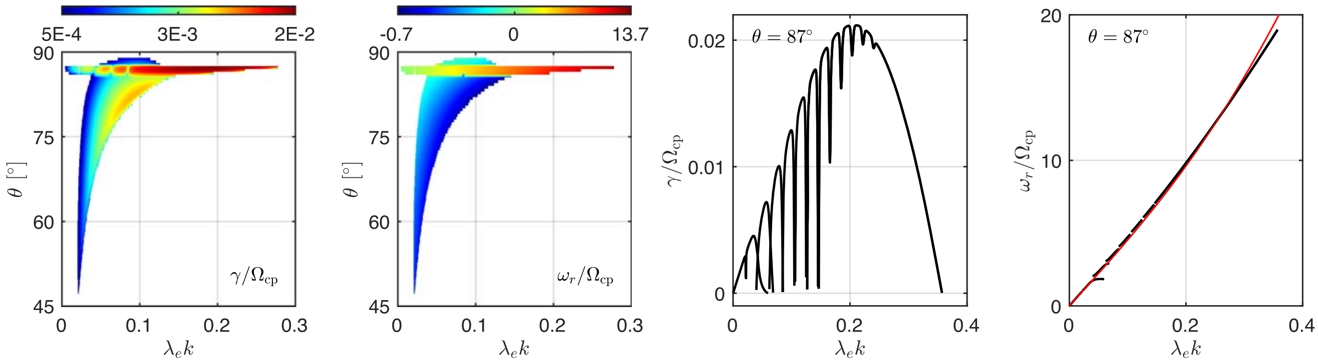

(b) Energy transfer rates at different $n$ in LH-HFI: $\theta = 87°$

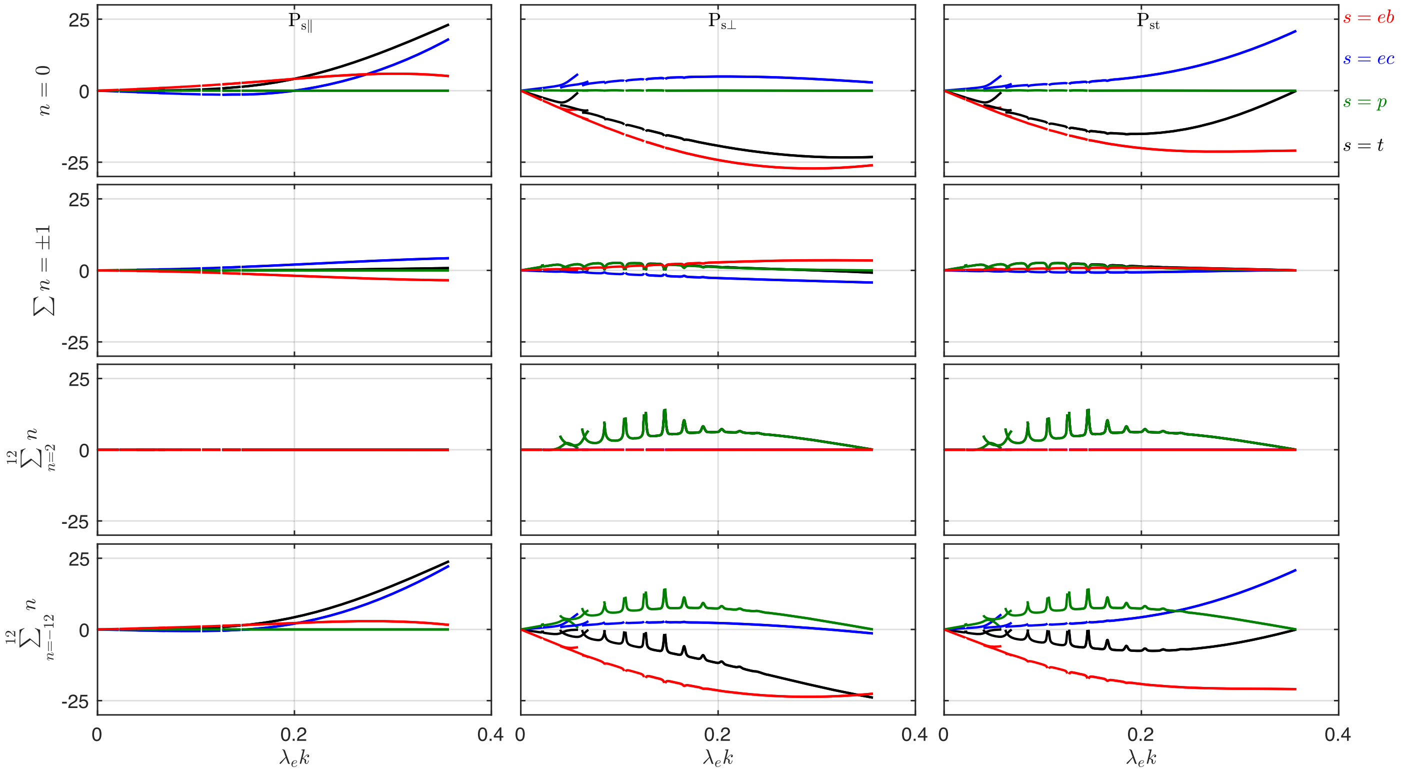

**Figure 4.** (a) Electron heat flux instability driven at $V_{\rm eb} = 1.5 \times 10^4$ km s$^{-1}$ and $r = 10R_S$: the $k - \theta$ distributions of the growth rate $\gamma$ and the real wave frequency $\omega_r$; and the distributions of $\gamma$ and $\omega_r$ at $\theta = 87°$, in which the red curve represents the dispersion relation of the fast-magnetosonic/whistler mode wave in the cold fluid model (Zhao 2015). (b) Energy transfer rates at different $n$ in LH-HFI triggered at $\theta = 87°$. The red, blue, and green curves denote energy transfers relating to the electron beam, electron core, and proton population, respectively, and the black curves represent the net energy transfer rate.

resonance interactions between protons and lower-hybrid waves (see Figure 4(b)). We note that a good consistence between the dispersion relation of unstable waves in LH-HFI and the dispersion relation of fast-magnetosonic/whistler waves in the cold plasma model (red curve in Figure 4(a); Zhao 2015) clarifies the mode nature of unstable waves again.

Figure 4(b) presents energy transfer rates at different $n$ in LH-HFI, which are useful in exploring exact wave-particle interaction mechanism associating with the resonant condition $\omega = k_\| v_{s\|} + n\Omega_{\rm cs}$ through the energy transfer method (e.g., Stix 1992; Quataert 1998; He et al. 2019). The most interesting finding is that the wave-particle interaction relating to perpendicular electric field and $n = 0$ resonant beam electrons is main source to drive LH-HFI, i.e., $P_{\rm eb\perp}(n = 0) < 0$. This is different from the argument of LH-HFI driven by the $n = 1$ resonance of beam electrons (Verscharen et al. 2019). $P_{\rm eb\perp}(n = 0) < 0$ indicates that transit-time resonant interactions are responsible for the excitation of LH-HFI (Stix 1992). Because the energy transfer between unstable waves and beam/core electrons at $n = 1$ is nearly totally compensated by the corresponding energy transfer at $n = -1$, the sum of energy transfer rates at $n = \pm 1$ is nearly zero, as shown in Figure 4(b). Moreover, Landau resonance interactions between unstable waves and $n = 0$ resonant beam electrons can induce a slight heating of the electron beam population in parallel direction. In addition, anomalous cyclotron-resonant interactions between unstable waves and $n = 1$, 2...12 resonant protons result in the energy flowing into protons from unstable waves, and the energy transfer rate significantly enhances at $\omega \simeq n\Omega_{\rm cp}$, which would induce the wave damping as shown in Figure 4(a).

In medium-$\beta_e$ plasma, PW-HFI is the only instability controlling the electron dynamics as $V_{\rm eb} < V_{\rm tran}$ (Figure 1; also see López et al. 2020; Sun et al. 2020). As the strongest unstable waves are parallel whistler waves having right-hand polarization, these waves interact with $n = -1$ resonant beam electrons at the resonant speed of $v_{\rm res} = (\omega + \Omega_{\rm ce})/k_\parallel < 0$ (e.g., Vasko et al. 2019; Verscharen et al. 2019), leading to the energy transport from the electron beam into unstable waves (Figure 1). Moreover, cyclotron wave-particle interactions between unstable waves and $n = -1$ resonant core electrons (with the same resonant speed as resonant beam electrons) can result in energy of unstable waves flowing into the electron core. Therefore, PW-HFI would scatter $n = -1$ resonant beam electrons toward smaller $v_\perp$and induce $n = -1$ resonant core electrons scattering into larger $v_\perp$in the eVDF.

## 4. Discussion and Summary

In this Letter we explored the electron heat flux instability as functions of $r$ and $V_{\rm eb}$ in the inner heliosphere. We exhibited that a large electron heat flux can destabilize electron acoustic waves as $V_{\rm eb} \gtrsim 1.3 V_{\rm Teb}$, lower-hybrid waves and oblique Alfvén waves at $r \lesssim 30 R_S$ as $V_{\rm eb} \lesssim 1.3 V_{\rm Teb}$, and parallel whistler waves at $r \gtrsim 10 R_S$ as $V_{\rm eb} \lesssim 1.3 V_{\rm Teb}$. Because different $r$ corresponds to different $\beta_e$, LH-HFI and OA-HFI arise as $\beta_{\rm ec} \lesssim 0.15$, and PW-HFI occurs as $\beta_{\rm ec} \gtrsim 0.06$. Due to the magnetic field and plasma parameters used in this study, we have $\beta_{\rm ec} < 1$. For high $\beta_e$ ($\gtrsim 1$) plasma environment, besides PW-HFI, OW-HFI can also arise as $V_{\rm eb} \lesssim \sqrt{2}\, V_{\rm Teb}$ (López et al. 2020).

Recently, a number of works proposed that OW-HFI can effectively constrain the electron heat flux and scatter the strahl into the halo in the solar wind (e.g., Roberg-Clark et al. 2018; Kuzichev et al. 2019; Vasko et al. 2019; Verscharen et al. 2019; López et al. 2020). As EA-HFI controls OW-HFI under the condition of isotropic temperatures in both core and beam populations at $V_{\rm eb} \gtrsim 1.3 V_{\rm Teb}$ (Figure 3; see also Sun et al. 2020), it is interesting to consider the problem of how OW-HFI becomes dominant in plasmas with $\beta_e < 1$. This study proposes a dynamical evolution process of both the heat flux instability and eVDF, which would be in favor of the excitation of OW-HFI. During and after EA-HFI, due to strong Landau-resonant interactions of quasi-electrostatic electron acoustic waves with electrons, the parallel temperatures of both core and beam electron populations increase, leading to appearance of the parallel temperature anisotropy in such two electron populations. In turn, EA-HFI is suppressed, and only OW-HFI survives. Moreover, due to strong growth rate ($\sim \Omega_{\rm pe}$), EA-HFI can reach saturation after a short time, and therefore the corresponding eVDF evolves very quickly. We note that the parallel heating of the electron population during EA-HFI has been confirmed through PIC simulations (Lee et al. 2019).

The electron parallel temperature anisotropy is an important parameter to enhance OW-HFI. However, in addition to EA-HFI, the adiabatic magnetic focusing and free streaming due to the electron temperature gradient can also be responsible for the electron parallel temperature anisotropy. Due to the thermal pressure gradient in the solar wind, a portion of electrons move anti-sunward along the interplanetary magnetic field. These escaping electrons conserve their magnetic moment $\mu = (m v_\perp^2/2)/B_0$, and they become gathering the magnetic field-aligned direction because of the interplanetary magnetic field strength $B_0$ decreasing with the heliocentric distance (e.g., Berčič & Maksimović et al. 2019). Consequently, these global effects may favor the excitation of OW-HFI in the solar wind.

This Letter also proposes that LH-HFI is not triggered by the anomalous cyclotron interaction of beam electrons. According to an elaborate analysis of energy transfer rates, the excitation of LH-HFI is mainly induced by wave-particle interactions relating to perpendicular electric field and $n = 0$ resonant beam electrons (transit-time interactions; see Stix 1992). Moreover, the cyclotron-resonant interactions between unstable lower-hybrid waves and protons at $\omega = n\Omega_{\rm cp}\,(n \neq 0)$ can induce significant heating of the proton population in perpendicular direction, which would contribute to the solar coronal heating. This prediction can be tested by the Parker Solar Probe when it encounters the solar atmosphere.

In addition to this, PW-HFI only scatters core and beam electrons propagating against the magnetic field (Verscharen et al. 2019; López et al. 2020). Therefore, as proposed by previous theoretical studies (e.g., Vasko et al. 2019; Verscharen et al. 2019; López et al. 2020) and PIC simulations (e.g., Roberg-Clark et al. 2018; Kuzichev et al. 2019), PW-HFI is incapable of scattering the strahl into halo in the solar wind.

Lastly, we note that this study conjectures the evolution of the eVDF based on the linear theory predictions. The quasi-linear theory can provide a more self-consistent procedure to predict the evolution of the eVDF through wave-particle interactions (e.g., Kennel & Engelmann 1966). Recently, Jeong et al. (2020) developed a quasi-linear diffusion model that can describe the general plasma wave instability, and they identified the scattering of $n = 1$ resonant strahl electrons into the halo during OW-HFI (Verscharen et al. 2019; López et al. 2020). This model can also be helpful for exploring the role of LH-HFI and other heat flux instabilities on the evolution of the eVDF.

This work was supported by the NNSFC 41974203, 41531071, and 11673069. The authors appreciate the referee's helpful suggestions and comments.

## ORCID iDs

Jinsong Zhao https://orcid.org/0000-0002-3859-6394
Wen Liu https://orcid.org/0000-0002-8376-7842
Yuriy Voitenko https://orcid.org/0000-0002-4139-1795
Viviane Pierrard https://orcid.org/0000-0001-5014-7682
Chen Shi https://orcid.org/0000-0002-9166-1036
Huasheng Xie https://orcid.org/0000-0001-9204-135X
Dejin Wu https://orcid.org/0000-0003-2418-5508

## References

An, X., Bortnik, J., Van Compernolle, B., et al. 2017, PhPl, 24, 072116
Bale, S. D., Goetz, K., Harvey, P. R., et al. 2016, SSRv, 204, 49
Berčič, L., Maksimović, M., et al. 2019, MNRAS, 486, 3404
Boldyrev, S., & Horaites, K. 2019, MNRAS, 489, 3412
Feldman, W. C., Asbridge, J. R., Bame, S. J., et al. 1974, RvGSP, 12, 715
Feldman, W. C., Asbridge, J. R., Bame, S. J., et al. 1975, JGR, 80, 4181
Gary, S. P., & Feldman, W. C. 1977, JGR, 82, 1087
Gary, S. P., Feldman, W. C., Forslund, D. W., et al. 1975, JGR, 80, 4197
Gary, S. P., Skoug, R. M., & Daughton, W. 1999, PhPl, 6, 2607
Halekas, J. S., Whittlesey, P., Larson, D. E., et al. 2020, ApJS, 246, 22
Halekas, J. S., Whittlesey, P. L., Larson, D. E., et al. 2021, A&A, 650, A15
He, J., Duan, D., Wang, T., et al. 2019, ApJ, 880, 121
Horaites, K., Astfalk, P., Boldyrev, S., et al. 2018, MNRAS, 480, 1499
Jeong, S.-Y., Verscharen, D., Wicks, R. T., et al. 2020, ApJ, 902, 128
Kennel, C. F., & Engelmann, F. 1966, PhFl, 9, 2377
Klein, K. G., Martinović, M., Stansby, D., et al. 2019, ApJ, 887, 234

Kuzichev, I. V., Vasko, I. Y., Rualdo Soto-Chavez, A., et al. 2019, ApJ, 882, 81

Lazar, M., Pierrard, V., Poedts, S., et al. 2020, A&A, 642, A130

Lee, S.-Y., Lee, E., & Yoon, P. H. 2019, ApJ, 876, 117

López, R. A., Lazar, M., Shaaban, S. M., et al. 2020, ApJL, 900, L25

López, R. A., Shaaban, S. M., Lazar, M., et al. 2019, ApJL, 882, L8

Maksimovic, M., Zouganelis, I., Chaufray, J.-Y., et al. 2005, JGRA, 110, A09104

Marsch, E. 2006, LRSP, 3, 1

Micera, A., Zhukov, A. N., López, R. A., et al. 2020, ApJL, 903, L23

Pierrard, V., Lazar, M., Poedts, S., et al. 2016, SoPh, 291, 2165

Pierrard, V., Lazar, M., & Schlickeiser, R. 2011, SoPh, 269, 421

Pierrard, V., Maksimovic, M., & Lemaire, J. 2001, Ap&SS, 277, 195

Pilipp, W. G., Miggenrieder, H., Montgomery, M. D., et al. 1987, JGR, 92, 1075

Pulupa, M. P., Bale, S. D., Salem, C., et al. 2014, JGRA, 119, 647

Quataert, E. 1998, ApJ, 500, 978

Roberg-Clark, G. T., Agapitov, O., Drake, J. F., et al. 2019, ApJ, 887, 190

Roberg-Clark, G. T., Drake, J. F., Swisdak, M., et al. 2018, ApJ, 867, 154

Shaaban, S. M., Lazar, M., & Poedts, S. 2018, MNRAS, 480, 310

Shaaban, S. M., Lazar, M., Yoon, P. H., et al. 2019, MNRAS, 486, 4498

Shi, C., Zhao, J., Sun, H., et al. 2020, ApJ, 902, 151

Spitzer, L., & Härm, R. 1953, PhRv, 89, 977

Stix, T. H. 1992, Waves in plasmas (New York: American Institute of Physics), 1992

Štverák, Š., Maksimovic, M., Trávníček, P. M., et al. 2009, JGRA, 114, A05104

Sun, H., Zhao, J., Liu, W., et al. 2020, ApJ, 902, 59

Sun, H., Zhao, J., Xie, H., et al. 2019, ApJ, 884, 44

Tong, Y., Bale, S. D., Chen, C. H. K., et al. 2015, ApJL, 804, L36

Vasko, I. Y., Krasnoselskikh, V., Tong, Y., et al. 2019, ApJL, 871, L29

Verscharen, D., Chandran, B. D. G., Jeong, S.-Y., et al. 2019, ApJ, 886, 136

Vocks, C., & Mann, G. 2003, ApJ, 593, 1134

Volokitin, A., & Krafft, C. 2004, PhPl, 11, 3165

Xie, H. 2019, CoPhC, 244, 343

Xie, H., Denton, R., Zhao, J., et al. 2021, arXiv:2103.16014

Zhao, J. 2015, PhPl, 22, 042115